



Article

Nitrogen Atom-Doped Layered Graphene for High-Performance CO₂/N₂ Adsorption and Separation

Weifeng Lyu ¹, Linghui Sun ¹, Lu Wang ¹, Zemin Ji ¹, Sainan Zhou ², Yong Chen ^{3,*}  and Xiaoqing Lu ^{2,*} 

¹ State Key Laboratory of Enhanced Oil Recovery, Research Institute of Petroleum Exploration & Development, CNPC, Beijing 100083, China; lengsnupc@163.com (W.L.); zhaizhai20212021@163.com (L.S.); xhl15621429029@163.com (L.W.); 15856956521@163.com (Z.J.)

² School of Materials Science and Engineering, China University of Petroleum, Qingdao 266580, China; zhousn@s.upc.edu.cn

³ School of Geosciences, China University of Petroleum, Qingdao 266580, China

* Correspondence: yongchenzy@upc.edu.cn (Y.C.); luxq@upc.edu.cn (X.L.)

Abstract: The development of high-performance CO₂ capture and separation adsorbents is critical to alleviate the deteriorating environmental issues. Herein, N atom-doped layered graphene (N-MGN) was introduced to form triazine and pyridine as potential CO₂ capture and separation adsorbents via regulation of interlayer spacings. Structural analyses showed that accessible surface area of the N-MGN is 2521.72 m² g⁻¹, the porosity increased from 9.43% to 84.86%. At ultra-low pressure, N-MGN_6.8 have exhibited a high CO₂ adsorption capacity of 10.59 mmol/g at 298 K and 0.4 bar. At high pressure, the absolute adsorption capacities of CO₂ in N-MGN_17.0 (40.16 mmol g⁻¹) at 7.0 MPa and 298 K are much larger than that of N-doping slit pore. At 298 K and 1.0 bar, the highest selectivity of CO₂ over N₂ reached up to ~133 in N-MGN_6.8. The research shows that N doping can effectively improve the adsorption and separation capacity of CO₂ and N₂ in layered graphene, and the interlayer spacing has an important influence on the adsorption capacity of CO₂/N₂. The adsorption heat and relative concentration curves further confirmed that the layered graphene with an interlayer spacing of 6.8 Å has the best adsorption and separation ability of CO₂ and N₂ under low pressure. Under high pressure, the layered graphene with the interlayer spacing of 17.0 Å has the best adsorption and separation ability of CO₂ and N₂.

Keywords: N doping; interlayer spacing; Grand Canonical Monte Carlo simulation; CO₂ capture and separation



Citation: Lyu, W.; Sun, L.; Wang, L.; Ji, Z.; Zhou, S.; Chen, Y.; Lu, X. Nitrogen Atom-Doped Layered Graphene for High-Performance CO₂/N₂ Adsorption and Separation. *Energies* **2022**, *15*, 3713. <https://doi.org/10.3390/en15103713>

Academic Editors: Yuhe Wang, Chiyu Xie, Jiulong Wang and Rouhi Farajzadeh

Received: 16 April 2022

Accepted: 6 May 2022

Published: 18 May 2022

Publisher's Note: MDPI stays neutral with regard to jurisdictional claims in published maps and institutional affiliations.



Copyright: © 2022 by the authors. Licensee MDPI, Basel, Switzerland. This article is an open access article distributed under the terms and conditions of the Creative Commons Attribution (CC BY) license (<https://creativecommons.org/licenses/by/4.0/>).

1. Introduction

With the rapid developing of economic and world population [1], global CO₂ emissions from flue gases [2] have exceed 32 Gt of CO₂ per year. The greenhouse effect, triggered by the fast accumulation of carbon dioxide (CO₂) [3] has caused a lot of harm to society, environment and healthy of human-beings [4]. Carbon capture and storage (CCS) technology is an effective method to decrease the concentration of CO₂ and alleviate the greenhouse effect [5]. For CCS, the efficiency of capture and separation of CO₂ is mainly determined by the performance of adsorbent [6]. Aqueous amine solutions [7] are widely used as practical materials for CCS. However, they suffer from high parasitic energy consumption, adverse environmental impact, solvent losses and corrosion issues [8]. Comparing to amine solutions, solid adsorbents have high working capacity and lower regeneration energy when applied to gas capture. Therefore, they have become promising candidates as a CO₂ adsorbent for CCS [9]. Hitherto, various materials have been developed as the solid adsorbent, such as carbonaceous porous materials, porous organic materials, covalent organic frameworks, metal organic frameworks, and molecular sieves. Among them, graphene with split pore, as a typical carbonaceous material, has been considered as an

ideal candidate because of its low density, high chemical stability, excellent processability, and eco-friendly behavior [10].

Many factors can affect graphene structures, such as electromagnetic radiation [11], external electric field [12], laser-induction [13], and chemical doping [14], and so on. To further improve the adsorption behavior of CO₂, nitrogen (N) doping was widely investigated experimentally and theoretically due to its ability to change the packing pattern of the adsorbate, as well as to enhance the interaction between gas and frameworks [15]. To et al. [16] synthesized N-doped hierarchical porous graphitic carbons with large surface area and pore size, which showed good working capacity and separation performance. This performance is ten times larger than most previously reported mesoporous carbon adsorption materials. Psarras and coworkers [17] evaluated the uptake of CO₂ and N₂ in N-doped carbon with slit pore, and discovered that N atoms doping have a positive effect on CO₂ loading and selectivity of CO₂ over N₂. Apart from N doping, the slit pore frameworks also play a decisive character on CO₂ capture and separation performance. Kumar et al. [18] adopted molecular simulations to investigate the carbon capture behavior in N doped graphitic carbons and uncovered that the structure with slit pores is superior to disordered ones on CO₂ adsorption. In spite of these findings, the influence of pore sizes and N doping on the CO₂ capture behavior in graphite slit pore remains unelucidated.

In this work, we shed lights on how the layer distance and N doping affect CO₂ capture and CO₂/N₂ separation selectivity in multilayer graphene sheets (N-MGNs) at room temperature. First, by density functional theory (DFT) simulations, unit cell structure optimization and atomic partial charge were calculated by which was the prior preparation for CO₂ capture and separation. Then, the physical structure of the N-MGNs were explored. Afterwards, the single-component adsorption of CO₂ or N₂ is calculated under different pressures. Next, essential mechanism of N-doping was explored by the radial distribution functions, isosteric heats, and gas distribution. In the end, the separation performance of CO₂ from mixture gases (CO₂:N₂ = 1:1) was calculated to investigate the influence of different compositions. Our results highlighted the positive effect of N doping on graphene sheets, and provide the high-performance adsorbent for CCS technology.

2. Model and Computing Methodology

The supercells of different N-doped multilayer graphene nanostructures (N-MGNs) were used in this work. As depicted in Figure 1, N-doped graphene was built with two different N atoms in the form of triazine and pyrazine as doping sites. This structure can be synthesized via a well-developed ionothermal technique. The doping model and synthetic method was chosen referring to the latest work of Zhu et al. [19]. After building the N-doped graphene, we adopted DFT simulations to optimize the single-layer N-MGN structure and calculated the atomic partial charge of N-MGNs. B3LYP/6-31+g(d,p) basis set in Gaussian 09 [20] package was applied, this choice is a combination of efficiency and accuracy of the calculations. The atomic partial charges of N-graphenes were the critical parameters in coulomb law to describe the electrostatic interaction between gas and frameworks. The layer distance (H), described as the length of the center of the upper and lower N-graphene plane was introduced to describe the morphology of the N-MGNs. Finally, five-layered N-MGNs, with the H varying from 3.4 to 17.0 nm in 3.4 Å increments, were designed to study the CO₂ adsorption capacity and separation properties. These structures were named as N-MGN_3.4, N-MGN_6.8, MGN_10.2, MGN_13.6 and MGN_17.0 according to H. For the N-MGNs frameworks, the universal force field (UFF) parameters were used to describe the non-coulomb interaction [21], which was successfully applied to carbon materials, zeolites and other similar systems. For CO₂ and N₂ molecules, three rigid linear models were used. The parameters of the molecules were adopted by TraPPE model [22]. Information of force field parameters and atomic partial charge of N-MGNs frameworks were listed in Table 1.

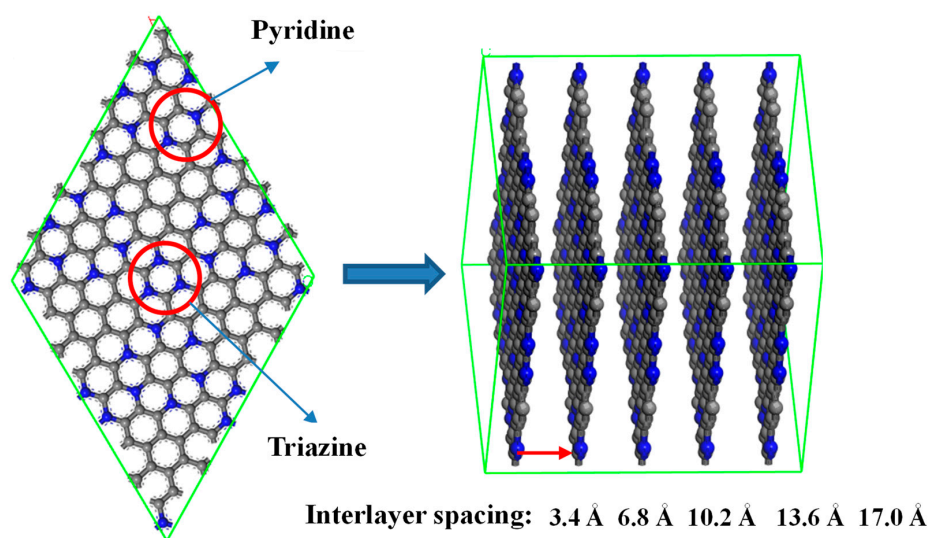


Figure 1. Initial configurations and frameworks of N-MGNs.

Table 1. Lennard-Jones parameters and atomic partial charges for CO₂, N₂, and N-MGNs.

Atom	Gas Molecule Models				MGNs Frameworks	
	C(CO ₂)	O(CO ₂)	N(N ₂)	COM(N ₂)	C	N
σ (Å)	2.08	3.05	3.31	0.00	3.43	3.26
ϵ (K)	27.00	79.00	36.00	0.00	52.84	34.72
q (e)	0.748	−0.374	−0.482	0.964	-	-

GCMC calculations were utilized to calculate the adsorptions together with the selectivity of CO₂ over N₂ [23]. This method is derived from the physical interaction between gases and frameworks. In GCMC simulations, a series of configurations would be generated randomly, including rotation, movement, and deletion [24]. In case of every state point, 1×10^7 steps were completed during GCMC calculation. An object-oriented multipurpose simulation code (MuSiC) was employed to complete CO₂ capture and separation [25].

3. Results and Discussions

3.1. Pore Topology and Morphology

Physical structure characteristics of pore are the major factors to influence capture and separation capacity of the adsorbent. To explore the physical properties of five N-MGNs, porosity (Φ) is calculated by V_P/V_{Total} , where V_P refers to pore size and V_{Total} is total volume of the N-MGNs. The parameters of the gas-accessible frameworks in Table 2 were obtained by Sarkisov [26] and Duren [27] methods. In case of slit pore, the limiting diameter and maximum diameter are nearly the same for each N-MGN, and the values are close to the corresponding layer distance. Accessible surface area of the five N-MGNs are exactly the same ($2521.72 \text{ m}^2 \text{ g}^{-1}$), because only the upper and lower surface of the five N-graphene sheets are exposed for all five N-MGNs. The accessible surface area is larger than many porous structures, such as zeolitic imidazolate frameworks ($620\text{--}1730 \text{ m}^2 \text{ g}^{-1}$) [28], some MOFs ($282\text{--}515 \text{ m}^2 \text{ g}^{-1}$) [29], some coordination polymers ($503\text{--}609 \text{ m}^2 \text{ g}^{-1}$) [30], and nanoporous organic frameworks ($\sim 1535 \text{ m}^2 \text{ g}^{-1}$) [31], [32], which could lead to superior adsorption capacity and selectivity. Different from the surface area, the porosity differs from each other for all N-MGNs. With the increase of layer distance, the porosity increased from 9.43% to 84.86%. N-MGN_{3.4} has ultra-small porosity of 9.43%, which lead to no adsorption capacity. N-MGN_{6.8} have moderate porosity of 54.72% which could result in better performance at low pressure. And the rest N-MGNs have higher porosity than 70%, which could achieve excellent performance at high pressure. Therefore, the five N-MGNs have great potentials to achieve excel CO₂ adsorption capacity.

Table 2. Pore physical characteristics of N-MGNs, gas probe molecule = He.

R	H_3.4	H_6.8	H_10.2	H_13.6	H_17.0
V_P (cm ³ /g)	0.04	0.461	0.882	1.307	1.727
Porosity, Φ (%)	9.43	54.72	72.71	77.49	84.86
D_L (Å)	0.95	3.90	6.94	10.71	13.68
D_M (Å)	0.97	3.96	7.11	10.80	13.76
Density g/cm ³	2.372	1.186	0.791	0.593	0.474
Accessible surface area (m ² /g)	2521.72	2521.72	2521.72	2521.72	2521.72

The geometric pore size distributions (PSDs) was shown in Figure 2 to investigate the pore morphology on step ahead. These data were obtained by Poreblazer v3.0 [33]. Helium was chose as the gas probe molecule. The results indicated that the PSDs peaks for the materials are narrow and independent due to the uniformly distributed pore sizes of slit pore. We found that the sum of the value of PSD peak and kinetic diameter of Helium (0.26 nm) is approximately equal to the corresponding layer distance. According to the IUPAC classification, N-NGM_3.6 and N-NGM_6.8 have ultramicropores (<7.00 Å), the other N-NGMs have micropores (7.00~20.00 Å) [34]. In summary, the pore spaces and diameters of N-MGNs were enhanced due to the increase of layer distance, particularly for N-NGMs NGM_3.4 and N-NGM_6.8. This can facilitate the gas adsorption and separation in gas-framework systems.

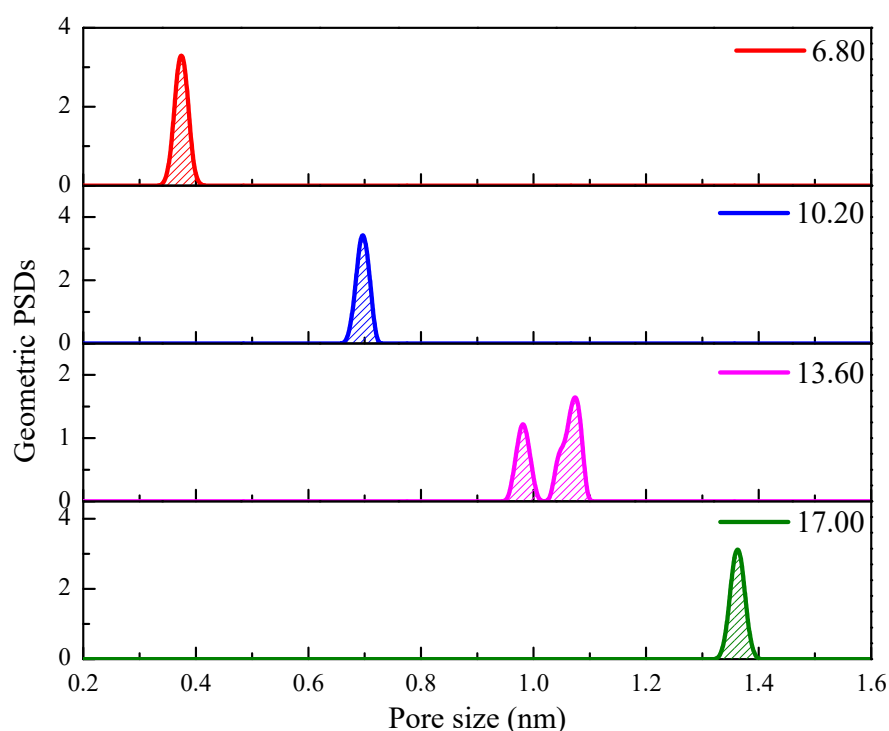
**Figure 2.** Pore size distributions of N-MGN with different interlayer distance.

Figure 3 shows the density of state (DOS) for N-NGMs, which analyzes orbital compositions of N-NGM. The result shows that N-NGM presents the typical metallic properties without band gaps. The total DOS of N-NGM consists of the p orbitals of the N and C atoms, and the peaks for these orbitals overlapped evidently, which indicates a strong bonding between the carbon and nitrogen in N-NGM.

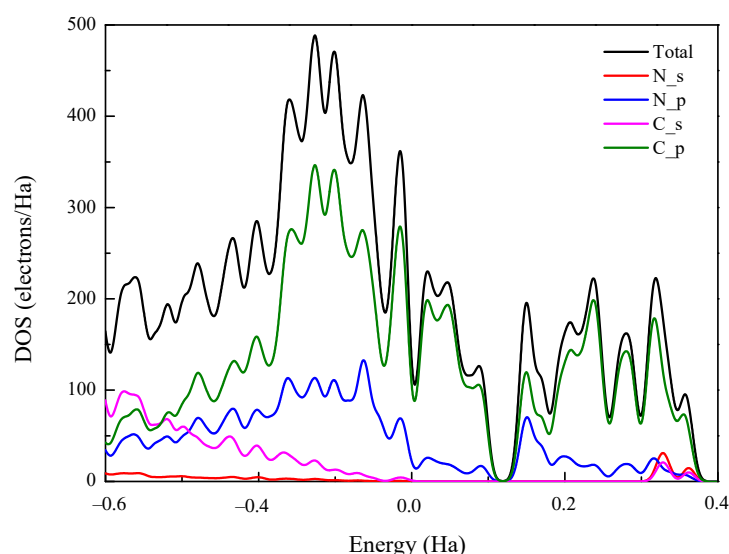


Figure 3. The density of state analyses of the N-MGN structures.

3.2. Single Component Adsorption of CO_2/N_2

One of the criterion factors to estimate adsorption capacity of the adsorbents is the absolute adsorption of gases, which were calculated by GCMC simulations in this work. Figure 4a,b shows the single component adsorption isotherms of CO_2 for N-MGNs in the range of 0–7.0 MPa, at 298 K. For N-MGN_3.4, the absolute adsorption capacity of CO_2 is 0, which suggested that no CO_2 could be adsorbed, because of the steric effect presented by the narrow interlayer spacing. At ultra-low pressure ($p < 0.04$ MPa), the adsorption capacity of CO_2 in the N-MGNs follows the sequence of $6.8 > 10.2 > 13.6 > 17.0 > 3.4$. The phenomenon can be explained that smaller pore sizes could lead to stronger CO_2 -frameworks interactions. Interestingly, the CO_2 uptake of N-MGNs_6.8 can rapidly reach to $10.59 \text{ mmol g}^{-1}$ at 0.04 MPa and 298 K, which is around 91.2% of the saturated capacity. The saturated pressure of N-MGNs_6.8 is smaller than that of SIFSIX-3-Cu [35], and larger than that of nanoporous carbons [36], which reflects a strong interaction between frameworks and gas molecules. At the pressure of 0.04–0.1 MPa, the CO_2 adsorption is in an order of $10.2 > 6.8 > 13.6 > 17.0 > 3.4$. This phenomenon is mainly because of the different pore sizes that cause the adsorption capacity of N-MGN_10.2 exceeding the saturation adsorption N-MGN_6.8 at low pressure. With continued growth of the pressure, the sequence of adsorption capacity for N-MGNs has changed. Under 0.1 MPa, the single component capacity of CO_2 in the N-MGN_6.8 is $10.70 \text{ mmol g}^{-1}$, which is greater than phosphorene slit pores ($\sim 1.5\text{--}5 \text{ mmol g}^{-1}$) [37], kgm-1-F (1.13 mmol/g) [38], C_3N pore (6.27 mmol/g) [39], S-graphite split pore ($36.48\text{--}51.00 \text{ mmol/mol}$) [40], graphene with different embedded surface functional groups ($\sim 1.0\text{--}9.0 \text{ mmol/g}$) [41], and carbon slit pores (~ 5 and 0.8 mmol g^{-1}) [41] at the similar conditions. When the pressure is over 4 MPa, CO_2 adsorption of N-MGNs follows the sequence of $17.0 > 13.6 > 10.2 > 6.8 > 3.4$ in Figure 4b, which is well match with the order of pore size. The situation clarified the fact that the adsorption capacity correlated with interaction strength at low pressure, while it correlated with free volumes at high pressure [42]. To evaluate the structural advantage, the N-MGNs were compared with N-doping materials with slit pore in Kumar's work [18]. The result shows that, at 0.1 MPa and 298 K, the absolute adsorption capacities of CO_2 in the N-MGNs_6.8 ($11.87 \text{ mmol g}^{-1}$) is much larger than that of N-doping slit pore with pore width of 0.8 nm (4.6 mmol g^{-1}). Moreover, at 7.0 MPa, the single component adsorption capacities of CO_2 in N-MGN_17.0 ($40.16 \text{ mmol g}^{-1}$) is much greater than N-doping slit pore with pore width of 2.0 nm ($\sim 16 \text{ mmol g}^{-1}$). This result confirms the adsorption advantage of our frameworks at both low and high pressure.

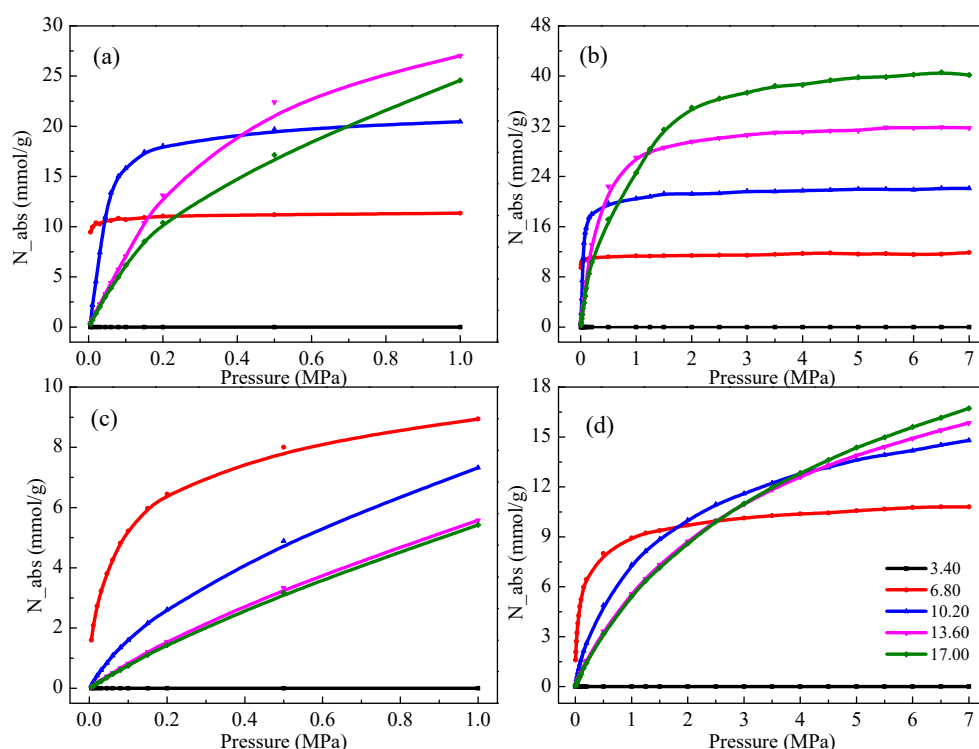


Figure 4. The absolute adsorption isotherms of CO₂ (a,b) and N₂ (c,d) at low and high pressure and 298 K.

Figure 4c,d delineate the single component adsorption isotherms of N₂ in the N-MGNs with different layer distance at 298 K. Moreover, the N-MGN_3.4 has no adsorption capacity in the pressure range of 0–7.0 MPa, because N₂ molecules can't get into the pore with relatively small pore size which is similar to CO₂ adsorption capacity. For other N-MGNs, the single component adsorption of N₂ follows the order of 6.8 > 10.2 > 13.6 > 17.0 at low pressure (0–1 MPa). This is because that the smaller pore size leads to the stronger interaction, which plays a critical role at low pressure. However, the adsorption changes upon the increase of pressure and it follows the consequence of 17.0 > 13.6 > 10.2 > 6.8 > 3.4 at 7 MPa. The type-I Langmuir adsorption behavior of CO₂/N₂ in N-MGNs demonstrate that the pore size of N-MGNs are typical micropores [43]. The result is consistent with the above-mentioned topology and morphology analysis of N-MGNs. Comparing with other materials, the N-MGNs could achieve preferable adsorption capacity of CO₂ at declined pressure, indicating the ability of N-MGNs to separate CO₂ from N₂.

3.3. Selectivity of CO₂ over N₂ with Equal Molar Fraction

The selectivity of CO₂ over impurity gases is of equal significance to evaluate adsorbent materials in CCS technology compared with the ability of CO₂ adsorption. Therefore, the selectivities of CO₂ over N₂ for all the N-MGNs were studied and defined as [36]:

$$S_{CO_2/N_2} = (x_{CO_2}/x_{N_2}) / (y_{CO_2}/y_{N_2}) \quad (1)$$

where S is the selectivity of CO₂ over N₂; x_{CO_2} and x_{N_2} are the molar fractions of CO₂ and N₂ in their adsorbed phase; and y_{CO_2} and y_{N_2} are the molar fractions. Figure 5 shows the selectivity of CO₂ over N₂ with 1:1 gas ratio for the N-MGNs at 298 K. Due to the non-adsorptive behavior for both CO₂ and N₂, N-MGN_3.4 is excluded in the selectivity study. In the above-mentioned range of pressures, the selectivities follow order of 6.8 > 10.2 > 13.6 > 17.0. The fact that increasing layer distance can reduce the S_{CO_2/N_2} , indicates that the layer distance has a significant influence on S_{CO_2/N_2} , especially at low pressure. The higher S_{CO_2/N_2} of N-MGN_6.8 is ascribed to the accessible N atoms and

suitable channel are the predominant factors for the remarkable selectivity of CO₂ over N₂. At equilibrium pressure, N-MGN_6.8 exhibits the highest selectivity (~133), which is superior to many N-doped mesoporous (~32) [44], pristine GY (~50) [45] and hierarchical (~21–67) [17] carbon adsorbents. Unlike isosteric heats of the N-MGNs, the sequence of the selectivity remains the same in case of all pressures. This finding further highlights that the N-MGNs show optimal S_{CO_2/N_2} in the mixture gas, especially for the one with a layer distance of 0.68 nm.

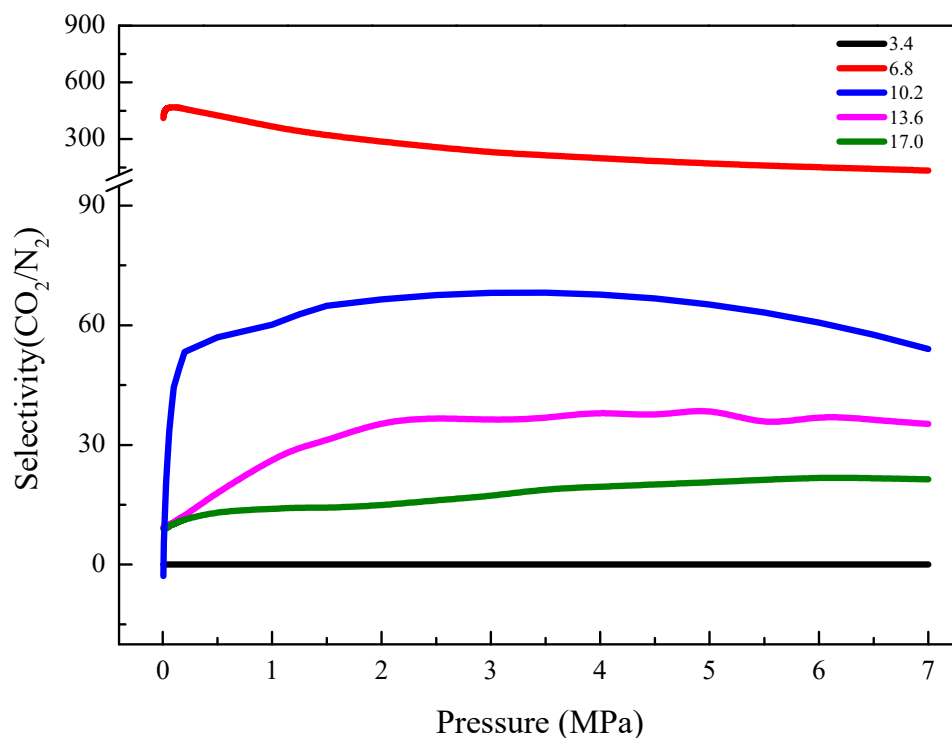


Figure 5. Selectivity of CO₂ over N₂ in N-MGNs at 298 K with equal ratio mixture ratios of CO₂/N₂.

3.4. Mechanism of CO₂/N₂ Adsorption in N-MGNs

Isosteric heats (Q_{st}). Q_{st} [46] is a benchmark to describe the interaction of adsorbing gas molecules and framework at a certain surface, which represents the affinity between gas molecules and frameworks. Q_{st} can be calculated from the Clausius–Clapeyron equation [47]. The Q_{st} of N-MGN_3.4 was not considered due to no adsorption of the gases. Figure 6a exhibits the relationship between Q_{st} and adsorption capacity of CO₂ at 298 K. At low pressure, the Q_{st} of CO₂ follows the order of 6.8 > 10.2 > 13.6 > 17.0, which is the same as the sequence of CO₂ adsorption. On the other hand, the isosteric heat profiles of N-MGNs_13.6 and N-MGNs_17.0 have three intersection points when the CO₂ uptake is lower than 12 mmol/g. This is because large pore sizes of N-MGNs_13.6 and N-MGNs_17.0 lead to weaker interactions at low pressure, thus resulting in little difference in the isosteric heat profiles. Therefore, the absolute adsorption isotherms of CO₂ for N-MGNs_1.36 and N-MGNs_1.70 nm almost overlapped at low pressure. The Q_{st} of CO₂ in N-MGNs_6.8 nm (~55 kJ mol⁻¹), is larger than edge-functionalized nanoporous carbons (24.63–34.25 kJ mol⁻¹), copper metal organic framework (~20 kJ mol⁻¹) [48], and SIFSIX-3-M series (~45–50 kJ mol⁻¹) [35]. It manifests the stronger interaction between CO₂ and N-MGNs, which leads to the larger adsorption capacity at low pressure than other adsorbent materials. For the N₂, the order of Q_{st} corresponds to the absolute adsorption capacity N₂, namely, 6.8 > 10.2 > 13.6 > 17.0 at low pressure (Figure 6b). The low Q_{st} of N₂ in N-MGNs_6.8 (~30 kJ mol⁻¹) indicates a typical weak physisorption of N₂. On the whole, the adsorption capacity of both CO₂ and N₂ are strongly related to the gas-framework interaction. And the stronger quadrupole moment of CO₂ indicates that CO₂ has the stronger interactions with N-MGNs than N₂.

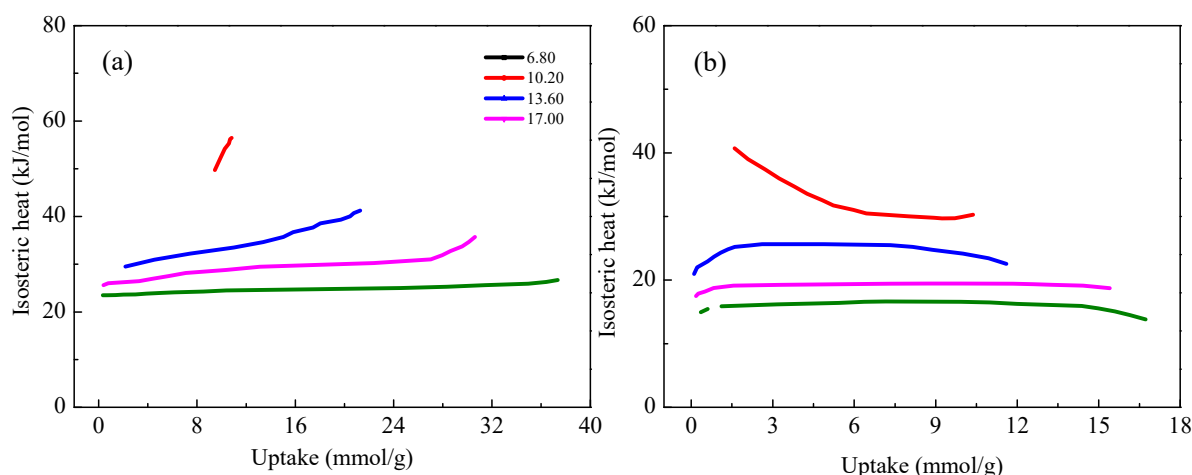


Figure 6. The isothermic heat of CO₂ (a) and N₂ (b) in the N-MGNs.

Gas distribution. To explore the gas distribution in equilibrium states for the pore of N-MGNs, the relative concentration profiles were presented as a function of the distance between layers. The relative concentration is defined as a ratio, that is calculated by dividing actual concentration by average concentration of the gas in the pore. The distribution of both CO₂ and N₂ in each layer of the N-MGNs can be reflected by relative concentration profiles. In most cases, it shows strong primary peaks close, minor secondary peaks, and bulk region [49]. The primary peak is resulted from the interaction between the first-layer of gas molecules adsorbed on the pore walls, that is, adsorbed phase. The secondary peak is mainly due to the equilibrating interactions between gas–gas or gas–surfaces, that is, equilibrated phase.

The relative concentration profiles of CO₂ in each layer of N-MGNs are shown in Figure 7a,d. For N-MGNs_{6.8}, an isolated and high primary peak appear in each layer, because the layer with narrow distance can only hold CO₂ molecules in the adsorbed phase. Moreover, the narrower layer distance leads to the overlap of two primary peaks for each pore. Differently, the two primary peaks were separated and next to each other for N-MGN_{10.2}. And in case of N-MGN_{13.6}, the equilibrated phase can be observed in between the two primary peaks. As for N-MGN_{17.0}, two primary peaks, two secondary peaks, and bulk region can be clearly visualized due to the large the enough space of each pore. The results explain the phenomenon that the N-MGN with larger layer distance have higher adsorption capacity at high pressure.

Figure 7e–h show that the relative concentration profiles of N₂ for the N-MGNs have similar trend as CO₂. When layer distance is narrow, only overlapped primary peaks can be seen. With the increase of layer distance, primary peaks separate and overlapped secondary peaks appear. When the layer distance reaches 1.70 nm, the integrated primary peaks, secondary peaks, and bulk region can be observed. However, the primary and secondary peaks of N₂ are inferior comparing to CO₂ due to the large kinetic diameter [50] and the stronger electric quadrupole moment of CO₂ molecule.

Overall, the relative concentration profiles visualized the distributions of gas molecules in each layer of N-MGNs. The results indicate that the layer distance is a significant factor to influence the adsorption capacity of CO₂/N₂ at high pressure, namely, the larger layer distance causes higher adsorption. This perfectly explains the change of the sequence of absolute adsorption isotherms at high pressure.

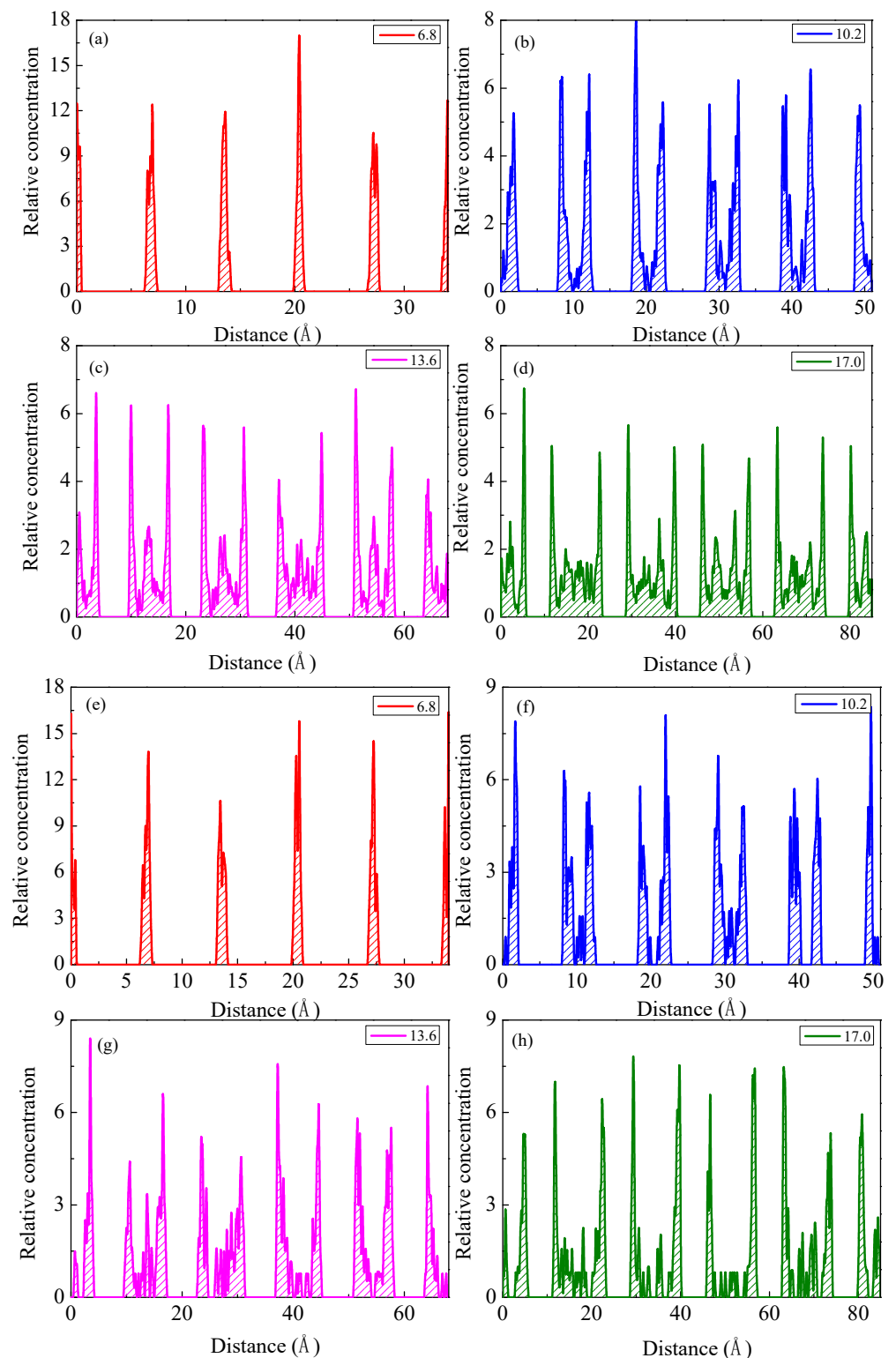


Figure 7. The relative concentration profiles of CO₂ (a–d) and N₂ (e–h) as a function of the layer distance in their equilibrium states.

4. Conclusions

The adsorption and separation behaviors of CO₂ and N₂ for N-MGNs with different layer distances were studied by simulations. Results have shown that the N-MGNs structure provides favorable pore space for CO₂ adsorption capacity and separation performance. At ultra-low pressure, N-MGN_{6.8} have shown an excellent CO₂ adsorption

behavior (10.59 mmol/g) at low pressure (0.4 bar). In comparison, the absolute adsorption of CO₂ for N-MGN_17.0 (40.16 mmol/g) at 7.0 MPa is much larger than that of N-doping slit pore under high pressures. At 1.0 bar, the highest S_{CO_2/N_2} reached up to ~133 in N-MGN_6.8. The adsorption heat and relative concentration curves confirm that the adsorption ability of CO₂ for the all the materials are better than that of N₂, and the change of the interlayer spacing has an important influence on the adsorption capacity of the gases. The effect has the advantage of adsorption. Under high pressure, the structure with large interlayer spacing has a strong adsorption capacity due to the large porosity. The five structures all showed strong CO₂/N₂ adsorption capacity at 0–7 MPa. This work highlights the advantages of CO₂/N₂ adsorption and separation in N-MGNs structure, as well as providing effective methods and strategies for the design and screening of high-quality adsorbate materials for carbon capture and storage technology.

Author Contributions: Formal analysis, L.W.; Funding acquisition, X.L.; Investigation, Y.C.; Resources, Z.J.; Software, L.S.; Writing—original draft, W.L.; Writing—review & editing, S.Z. All authors have read and agreed to the published version of the manuscript.

Funding: This work was supported by Shandong Natural Science Foundation, China (ZR2019MEM005), the Major Scientific and Technological Projects of CNPC (ZD2019–184-001), Teaching Reform Research Project of China University of Petroleum (ZY-202018), State Key Laboratory of Enhanced Oil Recovery of Open Fund Funded Project: (2022-KFKT-28), Major Special Projects of CNPC (2021ZZ01-03 and 2021ZZ01-05), Scientific and Technological Project of CNPC (2021DJ1103).

Institutional Review Board Statement: Not applicable.

Informed Consent Statement: Not applicable.

Data Availability Statement: Not applicable.

Conflicts of Interest: The authors declare no conflict of interest.

References

1. Pérez, S.; Del Molino, E.; Barrio, V.L. Modeling and Testing of a Milli-Structured Reactor for Carbon Dioxide Methanation. *Int. J. Chem. React. Eng.* **2019**, *17*. [[CrossRef](#)]
2. Yin, C.; Qiu, S.; Zhang, S.; Sher, F.; Zhang, H.; Xu, J.; Wen, L. Strength degradation mechanism of iron coke prepared by mixed coal and Fe₂O₃. *J. Anal. Appl. Pyrolysis* **2020**, *150*, 104897. [[CrossRef](#)]
3. Zhang, Y.; Fang, Y.; Jin, B.; Zhang, Y.; Zhou, C.; Sher, F. Effect of Slot Wall Jet on Combustion Process in a 660 MW Opposed Wall Fired Pulverized Coal Boiler. *Int. J. Chem. React. Eng.* **2019**, *17*. [[CrossRef](#)]
4. Cai, S.; Zhang, Y.; Wei, F.; Sher, L.; Wen, J.; Xu, J.; Dang, J.; Hu, L. A novel method for removing organic sulfur from high-sulfur coal: Migration of organic sulfur during microwave treatment with NaOH-H₂O₂. *Fuel* **2021**, *289*, 119800. [[CrossRef](#)]
5. Samanta, A.; Zhao, A.; Shimizu, G.K.H.; Sarkar, P.; Gupta, R. Post-Combustion CO₂ Capture Using Solid Sorbents: A Review. *Ind. Eng. Chem. Res.* **2011**, *51*, 1438–1463. [[CrossRef](#)]
6. Yu, J.; Xie, L.-H.; Li, J.-R.; Ma, Y.; Seminario, J.M.; Balbuena, P.B. CO₂ Capture and Separations Using MOFs: Computational and Experimental Studies. *Chem. Rev.* **2017**, *117*, 9674–9754. [[CrossRef](#)]
7. Dutcher, B.; Fan, M.; Russell, A.G. Amine-Based CO₂ Capture Technology Development from the Beginning of 2013—A Review. *ACS Appl. Mater. Interfaces* **2015**, *7*, 2137–2148. [[CrossRef](#)]
8. Mumford, K.A.; Wu, Y.; Smith, K.; Stevens, G.W. Review of solvent based carbon-dioxide capture technologies. *Front. Chem. Sci. Eng.* **2015**, *9*, 125–141. [[CrossRef](#)]
9. Huck, J.M.; Lin, L.-C.; Berger, A.H.; Shahrak, M.N.; Martin, R.L.; Bhowan, A.S.; Haranczyk, M.; Reuter, K.; Smit, B. Evaluating different classes of porous materials for carbon capture. *Energy Environ. Sci.* **2014**, *7*, 4132–4146. [[CrossRef](#)]
10. Lu, X.; Jin, D.; Wei, S.; Wang, Z.; An, C.; Guo, W. Strategies to enhance CO₂ capture and separation based on engineering absorbent materials. *J. Mater. Chem. A* **2015**, *3*, 12118–12132. [[CrossRef](#)]
11. Bludov, Y.V.; Peres, N.M.R.; I Vasilevskiy, M. Unusual reflection of electromagnetic radiation from a stack of graphene layers at oblique incidence. *J. Opt.* **2013**, *15*, 114004. [[CrossRef](#)]
12. Gong, C.; Lee, G.; Shan, B.; Vogel, E.; Wallace, R.; Cho, K. First-principles study of metal–graphene interfaces. *J. Appl. Phys.* **2010**, *108*, 123711. [[CrossRef](#)]
13. Ye, R.; James, D.K.; Tour, J.M. Laser-Induced Graphene: From Discovery to Translation. *Adv. Mater.* **2018**, *31*, e1803621. [[CrossRef](#)] [[PubMed](#)]
14. Liu, H.; Liu, Y.; Zhu, D. Chemical doping of graphene. *J. Mater. Chem.* **2011**, *21*, 3335–3345. [[CrossRef](#)]

15. To, J.W.F.; He, J.; Mei, J.; Haghpanah, R.; Chen, Z.; Kurosawa, T.; Chen, S.; Bae, W.-G.; Pan, L.; Tok, J.B.H.; et al. Hierarchical N-Doped Carbon as CO₂ Adsorbent with High CO₂ Selectivity from Rationally Designed Polypyrrole Precursor. *J. Am. Chem. Soc.* **2016**, *138*, 1001–1009. [[CrossRef](#)] [[PubMed](#)]
16. To, J.W.F.; Chen, Z.; Yao, H.; He, J.; Kim, K.; Chou, H.-H.; Pan, L.; Wilcox, J.; Cui, Y.; Bao, Z. Ultrahigh Surface Area Three-Dimensional Porous Graphitic Carbon from Conjugated Polymeric Molecular Framework. *ACS Cent. Sci.* **2015**, *1*, 68–76. [[CrossRef](#)]
17. Psarras, P.; He, J.; Wilcox, J. Molecular simulations of nitrogen-doped hierarchical carbon adsorbents for post-combustion CO₂ capture. *Phys. Chem. Chem. Phys.* **2016**, *18*, 28747–28758. [[CrossRef](#)]
18. Kumar, K.V.; Preuss, K.; Lu, L.; Guo, Z.X.; Titirici, M.M. Effect of Nitrogen Doping on the CO₂ Adsorption Behavior in Nanoporous Carbon Structures: A Molecular Simulation Study. *J. Phys. Chem. C* **2015**, *119*, 22310–22321. [[CrossRef](#)]
19. Zhu, X.; Tian, C.; Veith, G.M.; Abney, C.W.; Dehaut, J.; Dai, S. In Situ Doping Strategy for the Preparation of Conjugated Triazine Frameworks Displaying Efficient CO₂ Capture Performance. *J. Am. Chem. Soc.* **2016**, *138*, 11497–11500. [[CrossRef](#)]
20. Frisch, M.J.; Trucks, G.W.; Schlegel, H.B.; Scuseria, G.E.; Robb, M.A.; Cheeseman, J.R.; Scalmani, G.; Barone, V.; Mennucci, B.; Petersson, G.A.; et al. *01*; Gaussian, Inc.: Wallingford, CT, USA, 2009.
21. Rappe, A.K.; Casewit, C.J.; Colwell, K.S.; Goddard, W.A.; Skiff, W.M. UFF, a full periodic table force field for molecular mechanics and molecular dynamics simulations. *J. Am. Chem. Soc.* **1992**, *114*, 10024–10035. [[CrossRef](#)]
22. Potoff, J.J.; Siepmann, J.I. Vapor–liquid equilibria of mixtures containing alkanes, carbon dioxide, and nitrogen. *AIChE J.* **2001**, *47*, 1676–1682. [[CrossRef](#)]
23. Zhou, S.; Guo, C.; Wu, Z.; Wang, M.; Wang, Z.; Wei, S.; Li, S.; Lu, X. Edge-functionalized nanoporous carbons for high adsorption capacity and selectivity of CO₂ over N₂. *Appl. Surf. Sci.* **2017**, *410*, 259–266. [[CrossRef](#)]
24. Steele, W. Computer simulations of physical adsorption: A historical review. *Appl. Surf. Sci.* **2002**, *196*, 3–12. [[CrossRef](#)]
25. Gupta, A.; Chempath, S.; Sanborn, M.J.; Clark, L.A.; Snurr, R. Object-oriented Programming Paradigms for Molecular Modeling. *Mol. Simul.* **2003**, *29*, 29–46. [[CrossRef](#)]
26. Sarkisov, L.; Harrison, A. Computational structure characterisation tools in application to ordered and disordered porous materials. *Mol. Simul.* **2011**, *37*, 1248–1257. [[CrossRef](#)]
27. Düren, T.; Millange, F.; Férey, G.; Walton, A.K.S.; Snurr, R.Q. Calculating Geometric Surface Areas as a Characterization Tool for Metal–Organic Frameworks. *J. Phys. Chem. C* **2007**, *111*, 15350–15356. [[CrossRef](#)]
28. Phan, A.; Doonan, C.J.; Uribe-Romo, F.J.; Knobler, C.B.; O’Keeffe, M.; Yaghi, O.M. Synthesis, Structure, and Carbon Dioxide Capture Properties of Zeolitic Imidazolate Frameworks. *Acc. Chem. Res.* **2010**, *43*, 58–67. [[CrossRef](#)]
29. Li, Y.-W.; Yan, H.; Hu, T.-L.; Ma, H.-Y.; Li, D.-C.; Wang, S.-N.; Yao, Q.-X.; Dou, J.-M.; Xu, J.; Bu, X.-H. Two microporous Fe-based MOFs with multiple active sites for selective gas adsorption. *Chem. Commun.* **2017**, *53*, 2394–2397. [[CrossRef](#)]
30. Meza-Morales, P.J.; Gómez-Gualdrón, D.A.; Arrieta-Perez, R.R.; Hernández-Maldonado, A.J.; Snurr, R.Q.; Curet-Arana, M.C. CO₂ adsorption-induced structural changes in coordination polymer ligands elucidated via molecular simulations and experiments. *Dalton Trans.* **2016**, *45*, 17168–17178. [[CrossRef](#)]
31. Islamoglu, T.; Kim, T.; Kahveci, Z.; El-Kadri, O.M.; El-Kaderi, H.M. Systematic Postsynthetic Modification of Nanoporous Organic Frameworks for Enhanced CO₂ Capture from Flue Gas and Landfill Gas. *J. Phys. Chem. C* **2016**, *120*, 2592–2599. [[CrossRef](#)]
32. Kuchta, B.; Firllej, L.; Mohammadhosseini, A.; Boulet, P.; Beckner, M.; Romanos, J.; Pfeifer, P. Hypothetical High-Surface-Area Carbons with Exceptional Hydrogen Storage Capacities: Open Carbon Frameworks. *J. Am. Chem. Soc.* **2012**, *134*, 15130–15137. [[CrossRef](#)] [[PubMed](#)]
33. Di Biase, E.; Sarkisov, L. Systematic development of predictive molecular models of high surface area activated carbons for adsorption applications. *Carbon* **2013**, *64*, 262–280. [[CrossRef](#)]
34. Thommes, M.; Kaneko, K.; Neimark, A.V.; Olivier, J.P.; Rodriguez-Reinoso, F.; Rouquerol, J.; Sing, K.S.W. Physisorption of gases, with special reference to the evaluation of surface area and pore size distribution (IUPAC Technical Report). *Pure Appl. Chem.* **2015**, *87*, 1051–1069. [[CrossRef](#)]
35. Ziaee, A.; Chovan, D.; Lusi, M.; Perry, J.J.; Zaworotko, M.J.; Tofail, S.A.M. Theoretical Optimization of Pore Size and Chemistry in SIFSIX-3-M Hybrid Ultramicroporous Materials. *Cryst. Growth Des.* **2016**, *16*, 3890–3897. [[CrossRef](#)]
36. Lu, X.; Jin, D.; Wei, S.; Zhang, M.; Zhu, Q.; Shi, X.; Deng, Z.; Guo, W.; Shen, W. Competitive adsorption of a binary CO₂-CH₄ mixture in nanoporous carbons: Effects of edge-functionalization. *Nanoscale* **2015**, *7*, 1002–1012. [[CrossRef](#)]
37. Zhang, Y.; Liu, C.; Hao, F.; Xiao, H.; Zhang, S.; Chen, X. CO₂ adsorption and separation from natural gas on phosphorene surface: Combining DFT and GCMC calculations. *Appl. Surf. Sci.* **2017**, *397*, 206–212. [[CrossRef](#)]
38. Leng, X.L.Z. Investigation on CO₂ Adsorption and Separation over N₂ in Functionalized Metal-organic Framework. *J. Liaocheng Univ.* **2022**, *35*, 28–33.
39. Li, X.; Zhu, L.; Xue, Q.; Chang, X.; Ling, C.; Xing, W. Superior Selective CO₂ Adsorption of C₃N Pores: GCMC and DFT Simulations. *ACS Appl. Mater. Interfaces* **2017**, *9*, 31161–31169. [[CrossRef](#)]
40. Li, X.; Xue, Q.; Chang, X.; Zhu, L.; Ling, C.; Zheng, H. Effects of Sulfur Doping and Humidity on CO₂ Capture by Graphite Split Pore: A Theoretical Study. *ACS Appl. Mater. Interfaces* **2017**, *9*, 8336–8343. [[CrossRef](#)]
41. Liu, Y.; Wilcox, J. Effects of Surface Heterogeneity on the Adsorption of CO₂ in Microporous Carbons. *Environ. Sci. Technol.* **2012**, *46*, 1940–1947. [[CrossRef](#)]

42. Yang, Z.; Peng, X.; Cao, D. Carbon Dioxide Capture by PAFs and an Efficient Strategy To Fast Screen Porous Materials for Gas Separation. *J. Phys. Chem. C* **2013**, *117*, 8353–8364. [[CrossRef](#)]
43. Balbuena, P.B.; Gubbins, K.E. Theoretical interpretation of adsorption behavior of simple fluids in slit pores. *Langmuir* **1993**, *9*, 1801–1814. [[CrossRef](#)]
44. Bao, S.-J.; Krishna, R.; He, Y.-B.; Qin, J.-S.; Su, Z.-M.; Li, S.-L.; Xie, W.; Du, D.-Y.; He, W.-W.; Zhang, S.-R.; et al. A stable metal–organic framework with suitable pore sizes and rich uncoordinated nitrogen atoms on the internal surface of micropores for highly efficient CO₂ capture. *J. Mater. Chem. A* **2015**, *3*, 7361–7367. [[CrossRef](#)]
45. Zhou, S.; Wang, M.; Wei, S.; Cao, S.; Wang, Z.; Liu, S.; Sun, D.; Lu, X. First-row transition-metal-doped graphyne for ultrahigh-performance CO₂ capture and separation over N₂/CH₄/H₂. *Mater. Today Phys.* **2021**, *16*, 100301. [[CrossRef](#)]
46. Choma, J.; Stachurska, K.; Marszewski, M.; Jaroniec, M. Equilibrium isotherms and isosteric heat for CO₂ adsorption on nanoporous carbons from polymers. *Adsorption* **2016**, *22*, 581–588. [[CrossRef](#)]
47. Cimino, R.T.; Kowalczyk, P.; Ravikovitch, P.I.; Neimark, A.V. Determination of Isosteric Heat of Adsorption by Quenched Solid Density Functional Theory. *Langmuir* **2017**, *33*, 1769–1779. [[CrossRef](#)]
48. Liu, X.; Xiao, Z.; Xu, J.; Xu, W.; Sang, P.; Zhao, L.; Zhu, H.; Sun, D.; Guo, W. A NbO-type copper metal-organic framework decorated with carboxylate groups exhibiting highly selective CO₂ adsorption and separation of organic dyes. *J. Mater. Chem. A* **2016**, *4*, 13844–13851. [[CrossRef](#)]
49. Ambrose, R.J.; Hartman, R.C.; Campos, M.D.; Akkutlu, I.Y.; Sondergeld, C.H. Shale Gas-in-Place Calculations Part I: New Pore-Scale Considerations. *SPE J.* **2012**, *17*, 219–229. [[CrossRef](#)]
50. Sang, P.; Zhao, L.; Xu, J.; Shi, Z.; Guo, S.; Yu, Y.; Zhu, H.; Yan, Z.; Guo, W. Excellent membranes for hydrogen purification: Dumbbell-shaped porous γ -graphynes. *Int. J. Hydrogen Energy* **2017**, *42*, 5168–5176. [[CrossRef](#)]